PHYSICAL REVIEW E **88**, 033011 (2013)

Dynamical-systems analysis and unstable periodic orbits in reacting flows behind symmetric bluff bodies

Jia-Chen Hua and Gemunu H. Gunaratne
Department of Physics, University of Houston, Houston, Texas 77204, USA

Stanislav Kostka and Naibo Jiang
Spectral Energies, LLC, Dayton, Ohio 45434, USA

Barry V. Kiel and James R. Gord
Aerospace Systems Directorate, Air Force Research Laboratory, WPAFB, Ohio 45433, USA

Sukesh Roy[*]
Spectral Energies, LLC, Dayton, Ohio 45434, USA

(Received 21 May 2013; published 18 September 2013)

Dynamical systems analysis is performed for reacting flows stabilized behind four symmetric bluff bodies to determine the effects of shape on the nature of flame stability, acoustic coupling, and vortex shedding. The task requires separation of regular, repeatable aspects of the flow from experimental noise and highly irregular, nonrepeatable small-scale structures caused primarily by viscous-mediated energy cascading. The experimental systems are invariant under a reflection, and symmetric vortex shedding is observed throughout the parameter range. As the equivalence ratio—and, hence, acoustic coupling—is reduced, a symmetry-breaking transition to von Karman vortices is initiated. Combining principal-components analysis with a symmetry-based filtering, we construct bifurcation diagrams for the onset and growth of von Karman vortices. We also compute Lyapunov exponents for each flame holder to help quantify the transitions. Furthermore, we outline changes in the phase-space orbits that accompany the onset of von Karman vortex shedding and compute unstable periodic orbits (UPOs) embedded in the complex flows prior to and following the bifurcation. For each flame holder, we find a single UPO in flows without von Karman vortices and a pair of UPOs in flows with von Karman vortices. These periodic orbits organize the dynamics of the flow and can be used to reduce or control flow irregularities. By subtracting them from the overall flow, we are able to deduce the nature of irregular facets of the flows.

DOI: 10.1103/PhysRevE.88.033011 PACS number(s): 47.70.Pq, 47.27.De, 47.27.ed, 47.32.cb

I. INTRODUCTION

High-Reynolds-number fluid flow [1,2] and high-momentum combustion [3] are complex flows that couple dynamics on multiple spatial and temporal scales. Typically, large-scale structures are generated by external driving, and small-scale aspects are initiated by energy cascading [1,2]. These small-scale features are highly sensitive to initial conditions and tiny disturbances and exhibit irregular, nonrepeatable behavior; in addition, they affect the large-scale structures via feedback, thus complicating the overall flow as well as its analysis. This sensitive dependence on initial conditions, coupled with the nonlinearity of the underlying physical systems, makes it extremely difficult to conduct theoretical or computational analyses of flows [4,5]. An alternative approach is to conduct a modal decomposition of experimental data and develop phenomenological models for the flows. The high-resolution, high-frequency data needed for such analyses is becoming more readily available with advances in technology [6]. In this paper, we introduce an approach whereby modal decomposition can be used for phase-space reconstruction and dynamical systems analysis to study large-scale flow and bifurcations therein as well as to extract characteristics of noise and irregular facets of the flows.

The application reported here is for flame-shedding dynamics in high-momentum bluff-body-stabilized flames that are transitioning from near-blow-off to stable and acoustically coupled conditions [6–9]. The control parameter in the experiment is the equivalence ratio ϕ; i.e., the fuel-to-oxidizer ratio and the corresponding stoichiometric value. The physical systems analyzed are symmetric under reflection about a line parallel to the flows, and symmetric vortex shedding [10,11] is observed in the entire range of control parameters. As the equivalence ratio is reduced, the flows develop, in addition, the asymmetric von Karman vortices [6]. The approach outlined here, an extension of the principal-components analysis of Ref. [6], is geared toward the determination of the onset and characterization of the growth of von Karman vortices.

Acoustic instabilities can occur in a combustion environment when heat release and pressure fluctuations become coupled and exceed the system damping [3]. We employ bifurcation diagrams [12] and Lyapunov exponents [13] to quantify the shedding transitions for different flame holders. The information can be used to select flame holders that yield stable flow patterns under modifications in the upstream conditions. Such analyses may be valuable for bluff-body applications where a gross change in behavior is undesirable.

We also compute recurrent (or periodic) orbits embedded in the (state-space) neighborhood of the flows. It has been asserted, and demonstrated through examples, that chaotic motions are dense with unstable recurrent orbits [14–17] and

---

[*] Corresponding author: sroy@woh.rr.com

that dynamical invariants of the chaotic motion can be derived from the eigenvalues of these cycles [14,18–21]. The chaotic motion approaches a cycle, follows it closely for some time before moving away, returns close to another cycle, and the process is repeated. In this sense, irregular flows are organized around a "skeleton" of unstable cycles. Methods to extract periodic orbits from chaotic signals and spatiotemporally chaotic flows have been introduced [15,22] and used to analyze experimental time series [23–25].

The experiment is described briefly in Sec. II. In particular, we discuss possible sources of irregularity in the flow and highlight the presence of rapidly evolving small-scale structures. The analysis is presented in detail for flow across a bluff body in the shape of a v-gutter, and results for the remaining shapes are outlined in Sec. VII. The first step in the analysis, given in Sec. III, is a preliminary temporal or spatial filtering of the flow. In Sec. IV principal-components analysis [26–33] and symmetry are used to eliminate some irregular facets and establish the modes associated with the flow. In Sec. V we propose a method to quantify the magnitude of the von Karman modes and present the bifurcation diagram in terms of ϕ. We also discuss the dynamics in a reduced phase space and qualitative changes that accompany the onset of von Karman vortices. Section VI presents the computation of periodic orbits embedded in the flow and their use in characterizing the noise and small-scale irregular facets of the flow. The implications of our analysis are discussed in the concluding section.

II. EXPERIMENT

Flame studies were conducted within an optically accessible, atmospheric-pressure combustion test section that contains a bluff-body flame holder for flame stabilization. Air is delivered into a 152 × 127 mm rectangular test section at a constant rate of 0.32 kg/s. While the air rate is maintained constant, propane fuel is added and mixed upstream of the flame holder to provide equivalence ratios that vary between $\phi = 0.6$ and 1.1. The flame holder is a v-gutter with a width of 38.1 mm and an angle of 35°, which is capable of holding the flame to a blow-off equivalence ratio of $\phi = 0.55$. Additional facility details and detailed flame-holder dimensions are provided in Ref. [6].

Flame-shedding behavior within the test section was studied using high-speed chemiluminescence imaging. Imaging was performed to capture the axial plane of the flames in such a way that the reaction fronts, recirculation zone, and reactant regions could be viewed simultaneously. The imaging setup is shown in Fig. 1. A Phantom v7.1 camera is used to collect the chemiluminescence emitted from the test section by viewing the axial plane through an angled mirror. This stainless steel mirror with MgF_2 coating provides maximum reflection of emission from 300 to 900 nm and is required for imaging because of space limitations. The camera is equipped with a monochrome CMOS detector set to capture images with a resolution of 496 × 344 pixels at a rate of 10 kHz. The detector is sensitive only to light ranging from 400 to 900 nm. Therefore OH* chemiluminescence is not collected, while CH* and black-body radiation from soot are captured. An 85-mm Nikkor lens with an f-stop of 1.4 is coupled to the camera, resulting in a field of view of 165 × 102 mm within the test section.

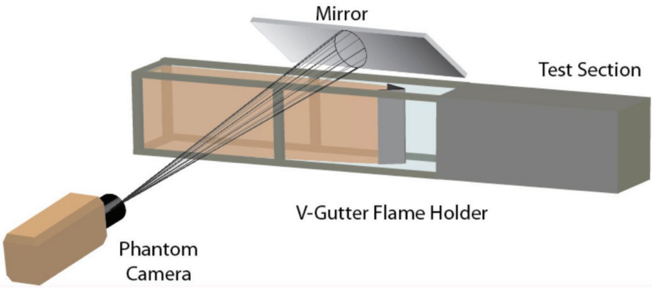

FIG. 1. (Color online) Side view of imaging setup with Phantom v7.1 high-speed camera and mirror.

For the present study, imaging of the chemiluminescence from the flame fronts is assumed to be an adequate representation of the flame-shedding mechanism. However, we should point out two drawbacks associated with this technique. First, when imaging flames at reduced equivalence ratios, signals decrease as emission from soot and CH* is reduced. Although higher camera sensitivity at short wavelengths and enhanced signal could be achieved by increasing the exposure time, the camera has an inherent 95-ms frame rate. Since image intensifiers often compromise spatial resolution, we refrain from using them in an attempt to retain as much flame-shedding structure as possible. Signal-to-noise ratios along the reaction front varied from ∼10 to ∼20 when the equivalence ratio was changed from $\phi = 0.6$ to 1.1.

The second drawback of chemiluminescence imaging is that signals are collected over a line-of-sight and cannot typically be extended to three dimensions. The current experiment aimed to minimize these effects by establishing, as far as possible, inlet conditions that were uniform along the depth axis; thus, the flame flow would be nearly two-dimensional. However, any nonuniformity in the fuel ratio or velocity field or symmetry breaking in the depth direction will result in slight asymmetries in the large structures of the flame. It should be noted that since turbulent flows are inherently three-dimensional, extremely small-scale structures along the shear layers will be captured in our two-dimensional images. Their collection along the line-of-sight of our imaging system will, therefore, contribute to measured flow irregularity and set a lower limit on the structural scales that can be analyzed.

III. TIME FILTERING

First, we perform a preliminary temporal filtering intended to reduce the small-scale structures in regions of large flow gradients. We assume, and the experiment verifies, that the onset and dynamics of these rapidly evolving structures are irregular and may be attributed to line-of-sight imaging effects from the experiment. To filter them, we consider the time sequence $f_{\mathbf{x}}(t) \equiv U(\mathbf{x},t)$ at a fixed location $\mathbf{x}$. Figure 2 displays the power spectrum of such a signal over 1 s of the flow (10 000 frames). The spectral components beyond 400 Hz appear to be irregular. Thus, we filter the signal using the filter

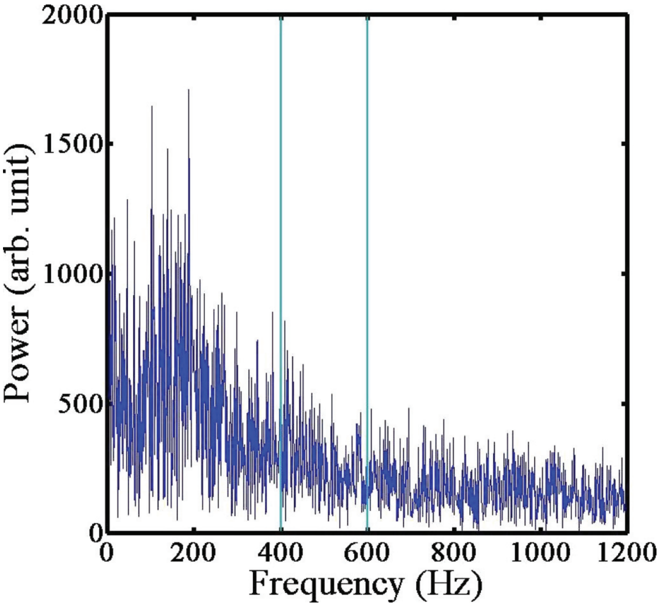

FIG. 2. (Color online) Power spectrum of time series for (chemiluminescence) intensities at a point **x** for flow at $\phi = 0.7$. Spectrum beyond 400 Hz does not appear to have a structure. Time filtering of the signal is implemented using the filter function given in Eq. (1).

function

$$\Theta(f) = \begin{cases} 1 & \text{if} \quad f \leqslant 400 \text{ Hz} \\ \frac{1}{2}\left[1 + \cos\pi\frac{f-400}{200}\right] & \text{if} \quad 400 \text{ Hz} < f \leqslant 600 \text{ Hz} \\ 0 & \text{if} \quad 600 \text{ Hz} < f \end{cases}, \tag{1}$$

which retains all spectral components below 400 Hz and smoothly reduces the fraction of spectral components until 600 Hz. The signal is then inverse Fourier transformed to obtain the filtered dynamics at **x**, and the time-filtered flow is constructed by combining the dynamics at all sites. Snapshots of the original and time-filtered flow at the 500th panel (0.05 s into the video), Fig. 3, show that some of the rapidly evolving, small-scale features of the flow have been eliminated.

Results of the analyses described below are robust against changes in the filter function. For example, none of the conclusions change if we shift the filter function by (say) 200 Hz. As $\Theta(f)$ is shifted more, it becomes progressively more difficult to compute periodic orbits of the flow.

We also implemented spatial filtering as follows: each snapshot was Fourier transformed, and the high wave-vector components filtered. The spatiotemporal dynamics are a composite of these spatially filtered images. The results from the analysis, including the coherent structures, bifurcation diagram, and periodic orbits are similar under temporal and spatial filtering. We also filtered the spatiotemporal dynamics both spatially and temporally and found comparable results.

IV. PRINCIPAL-COMPONENTS ANALYSIS

A. Preliminaries

For establishing the large-scale modes of the flow, it is necessary to reduce (or, if possible, eliminate) irregular small-scale features. We employed principal-components analysis (PCA) for this task [26–33]; its use is facilitated by the presence of a reflection symmetry in the system. Other approaches such as dynamic-mode decomposition [34,35] may be required for modal decomposition in systems with no such symmetry. The "data" consist of a video recording of the chemiluminescence of $N = 10\,000$ successive snapshots of the flow taken at 10 kHz. The analysis is conducted within a region defined by a height H (300 pixels; 100 mm) and a width W (200 pixels; 66 mm) behind the bluff body. We found that oscillations of the mean and standard deviation of the intensity in a frame were (nearly) commensurate with vortex shedding and that the results from the PCA improved when the frame intensities were normalized (to zero mean and unit variance). PCA was implemented on the normalized matrix $U(\mathbf{x},t)$ of N rows and $H \times W$ columns, where $\mathbf{x} = (x,y)$ and t is time. Here x represents the spanwise direction, and $y = 0$ is the central axis about which the system is reflection symmetric. In PCA this field is decomposed as

$$U(\mathbf{x},t) = \sum_{k=0}^{HW-1} a_k(t)\Phi_k(\mathbf{x}), \tag{2}$$

where $\Phi_k(\mathbf{x})$ $(k = 0,1,\ldots,HW-1)$ are referred to as the principal components or coherent structures and $a_k(t)$ are their time-dependent coefficients. $\Phi_0(\mathbf{x})$ is the time-averaged field. The coherent structures are normalized and form an orthonormal basis for expansion of the data. The terms in

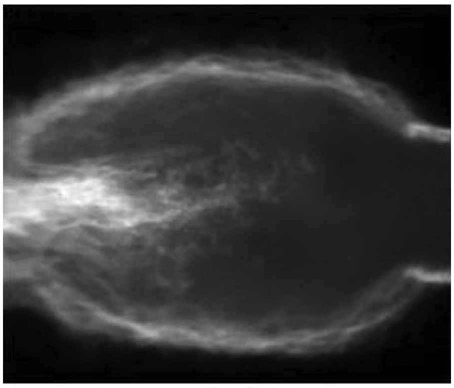

(a)

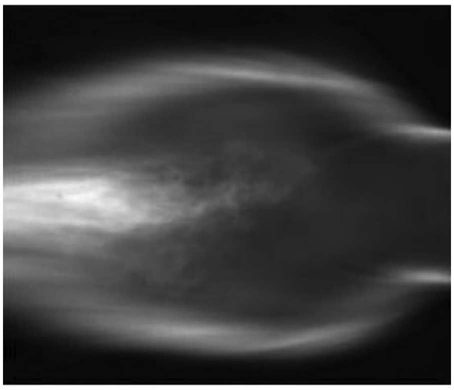

(b)

FIG. 3. The 500th panel of original and time-filtered flow, illustrating that the rapidly evolving small-scale motions have been filtered. Size of the images is approximately 100 × 66 mm.

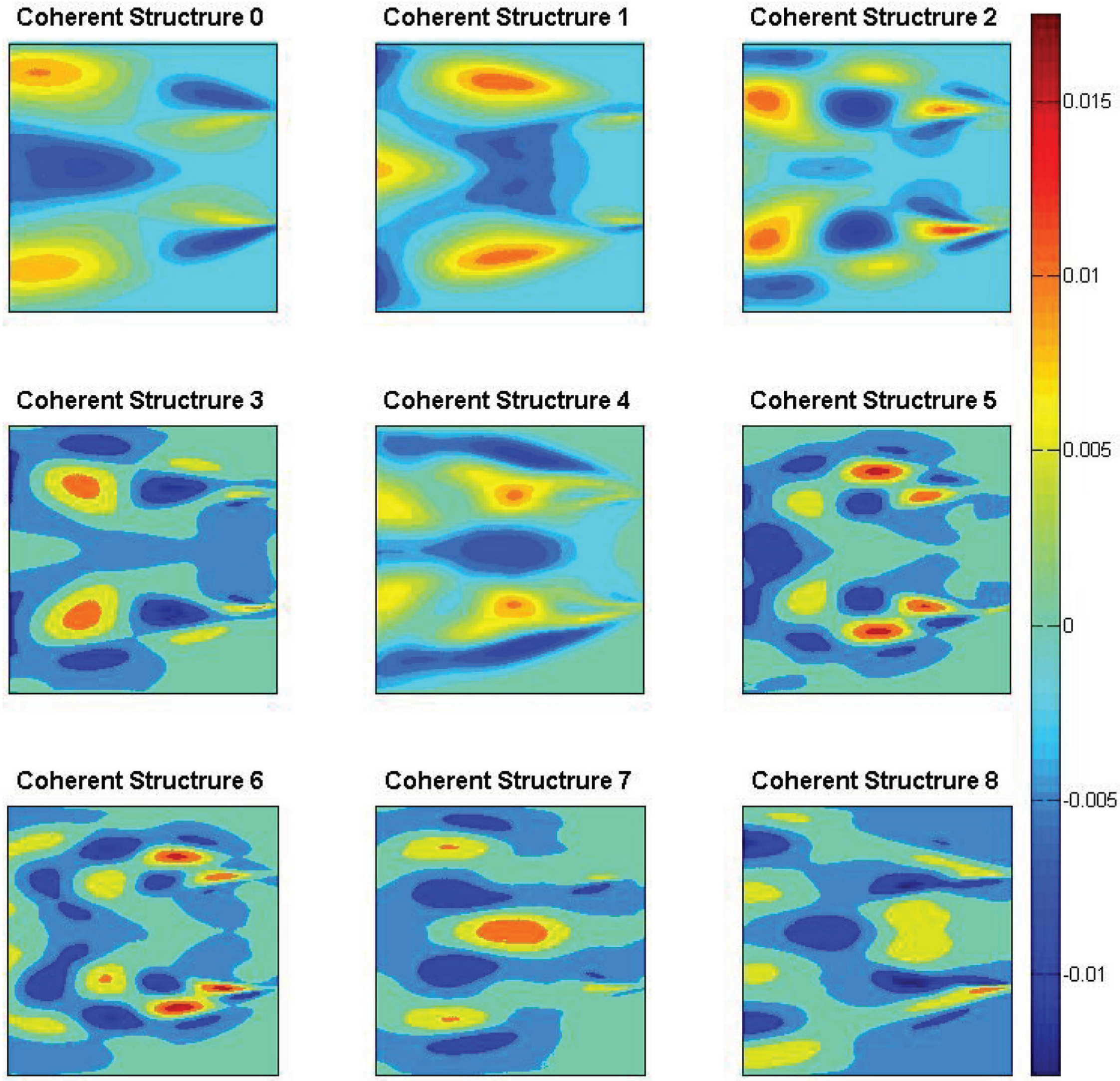

FIG. 4. (Color online) First nine coherent structures for flow at $\phi = 1.1$, all of which are nearly symmetric about the horizontal midline. Our analysis is predicated on the assumption that asymmetric components of these modes are due to slight experimental nonuniformities and dynamics of the small-scale irregular structures. The scale of individual images, and images in subsequent figures, is approximately 100 × 66 mm.

Eq. (2) are ordered such that their latencies (also referred to as "energies") $L_n = \langle a_n^2(t) \rangle$ are in nonincreasing order. A reduced-order model [36] for the flow can be derived by truncating the series (2) at an appropriate order N to obtain an approximation $U_N(\mathbf{x},t) \equiv \sum_{k=0}^{N-1} a_k(t)\Phi_k(\mathbf{x})$. The "quality" of the approximation is given by

$$\beta_N = \frac{\sum_{k=0}^{N-1} L_k}{\sum_{k=0}^{HW-1} L_k}. \tag{3}$$

Larger values of β_N correspond to better approximations of the data.

Two modes of flame shedding are well established in these reacting flows behind bluff bodies. In our experiments the more intense is that where a pair of vortices is simultaneously released from the sides of a symmetric bluff body [6]. The symmetry of the flow can be expressed in terms of the reflection operator $\mathcal{R} : (x,y) \to (x,-y)$ as

$$U(\mathcal{R}\mathbf{x},t) = U(\mathbf{x},t). \tag{4}$$

Now, the uniqueness of the principal-components expansion shows that for a symmetric flow field, $\Phi_n(\mathcal{R}\mathbf{x}) = \Phi_n(\mathbf{x})$ and, hence, that every coherent structure of the expansion is symmetric about the central axis [30,31].

The second mode of flame shedding is known as von Karman vortex shedding, where two vortices are shed asymmetrically; specifically, a vortex shed from one side of the bluff body is followed by one shed from the opposite side. The flow field $V(\mathbf{x},t)$ associated with von Karman shedding satisfies

$$V(\mathcal{R}\mathbf{x},t+T) = V(\mathbf{x},t), \tag{5}$$

where T is the time interval between successive shedding. If the vortices are shed periodically, T is constant. Because of the time delay T, the coherent structures for the flow are neither symmetric nor antisymmetric. However, in any (suitably filtered) flow comprises (only) symmetric and von Karman vortex shedding, nonsymmetric coherent structures are due to von Karman shedding. We assume that the intensity of the antisymmetric components is a measure of the strength of the latter.

B. PCA for flow at $\phi = 1.1$

Visually, the flow appears to involve only symmetric vortex shedding. The first nine coherent structures, all of which are nearly symmetric about the y axis, are shown in Fig. 4. We posit that the small asymmetry in these modes is not due to the large-scale flow but to experimental noise, irregularities from slight nonuniformities in the upstream inlet conditions, and/or deficiencies in the line-of-sight imaging. We introduce a symmetry-based method to filter some of these aspects.

The symmetric and antisymmetric components of the nth coherent structure $\Phi_n(x,y)$ are

$$\begin{aligned} &\Phi_{n,S}(\mathbf{x}) = \tfrac{1}{2}\,[\Phi_n(\mathbf{x}) + \Phi_n(\mathcal{R}\mathbf{x})]\,, \\ \text{and}\quad &\Phi_{n,A}(\mathbf{x}) = \tfrac{1}{2}\,[\Phi_n(\mathbf{x}) - \Phi_n(\mathcal{R}\mathbf{x})]\,, \end{aligned} \tag{6}$$

respectively. If our assumption is valid that the small asymmetry in the coherent structures is not due to large-scale flow, then the antisymmetric component $\langle|\Phi_{n,A}(x)|^2\rangle$ (1) would be small and (2) would be nearly unchanged between coherent structures. As is evident from Fig. 5, these expectations were indeed realized. The latency $\langle|\Phi_{n,S}(x)|^2\rangle$ of the symmetric components of the coherent structure decreases significantly with the mode number n, while that of $\langle|\Phi_{n,A}(x)|^2\rangle$ remains nearly unchanged. Furthermore, the fractional latency of $\langle|\Phi_{n,S}(x)|^2\rangle$ is larger by about a factor of 100 for the first few coherent structures. The difference decreases as n increases, signaling the enhanced role of noise (due to reductions in the latency of the coherent structures). Beyond $n \sim 15$, the latencies of the symmetric and antisymmetric components are similar, and the symmetric components are probably corrupted as well.

Note that we eliminate the antisymmetric components of the flow entirely in our analysis. Furthermore, we identify the cutoff in the PCA expansion by comparing the intensities of the symmetric and antisymmetric components. As discussed later in this paper, these modifications to the analysis of Ref. [6] provide a clear identification of the onset of von Karman vortex shedding.

C. PCA for flow at $\phi = 0.8$

Although the asymmetry in the flow is not easily observable, PCA selects modes that contain dominant antisymmetric components (see Fig. 6). The presence of the asymmetry implies that the motion contains structures outside of symmetric vortex shedding. The analyses of Sec. IV B show that the fractional latency of the antisymmetric components of Modes 5, 6, 9, and 12 is higher than those of the corresponding symmetric components (see Fig. 7). Again, we assume that the nondominant components are noise or irregular-motion generated and remove them from consideration.

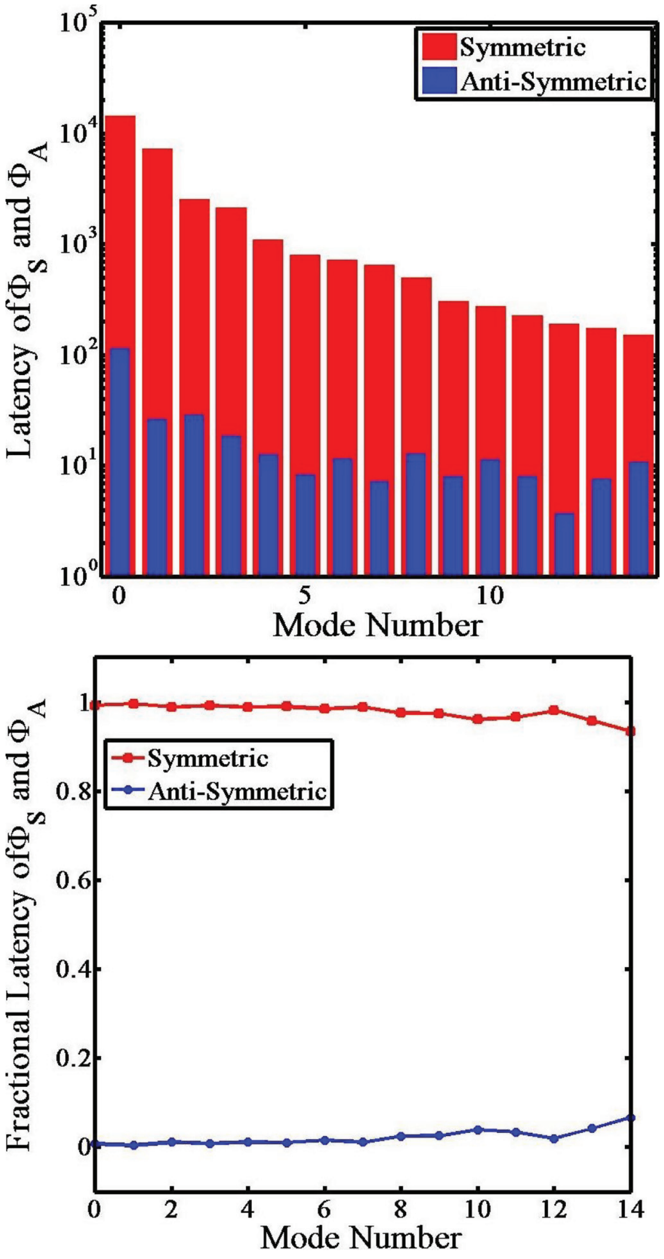

FIG. 5. (Color online) (a) Latency and (b) fractional latency of the symmetric (red) and antisymmetric (blue) components of the first 15 coherent structures. Observe that latencies of the antisymmetric components are small (by a factor of ~100) compared to those of the corresponding symmetric components. Furthermore, they remain nearly unchanged as the mode number n increases, supporting our assertion that the antisymmetric components are caused by experimental noise, irregular motions, and/or line-of-sight detection. The fractional latencies of the two components approach each other as n increases, indicating that, for large n, the symmetric components are corrupted as well.

V. ONSET OF VON KARMAN VORTICES: BIFURCATION DIAGRAM AND PHASE PORTRAITS

A. Bifurcation diagram

As discussed previously, in the absence of stochastic or irregular effects, the coherent structures of a flow that consists

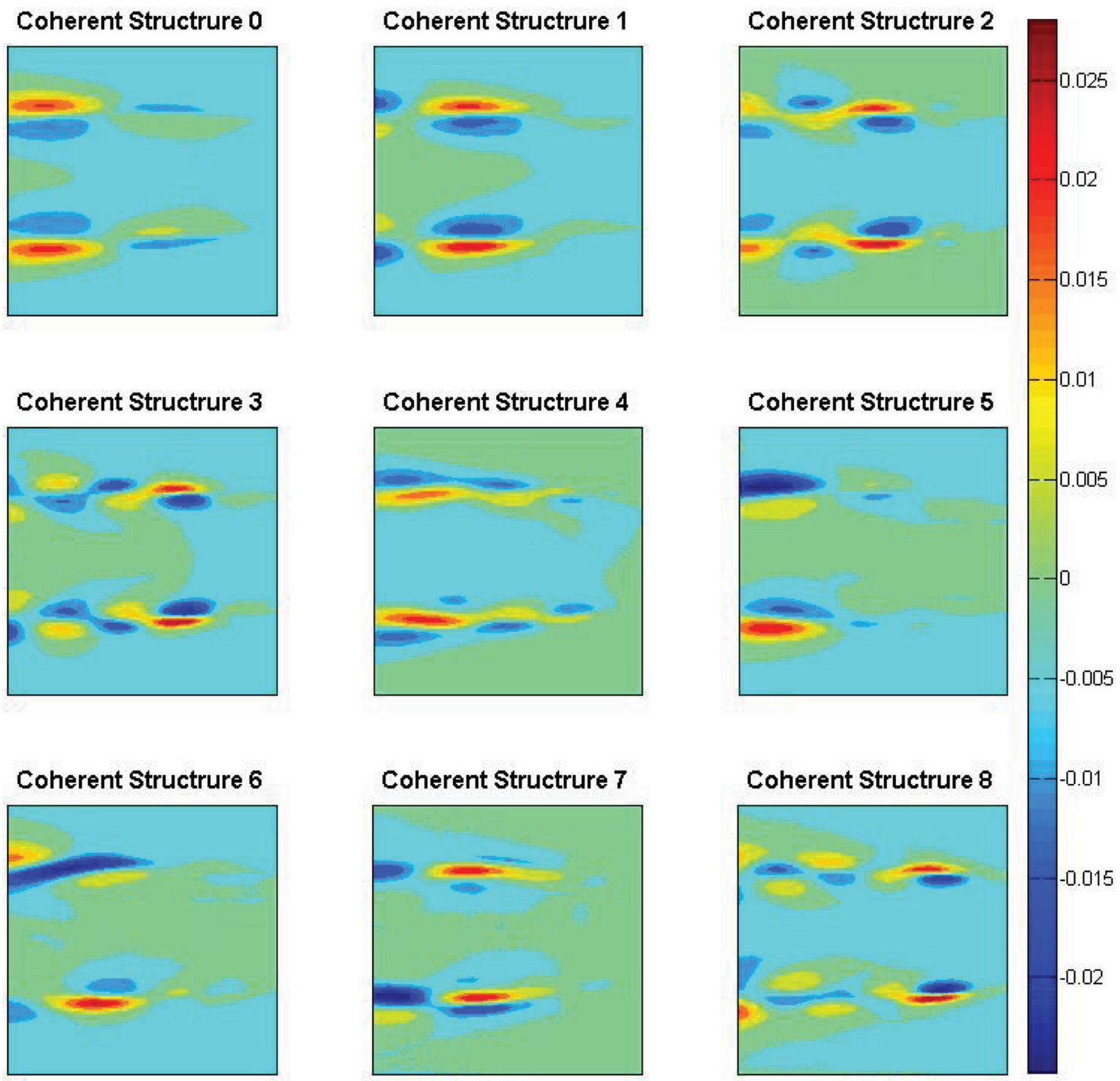

FIG. 6. (Color online) First nine coherent structures for flow at $\phi = 0.8$. Modes 5 and 6 (as well as 9 and 12, not pictured) appear to be primarily antisymmetric.

only of symmetric vortex shedding will be symmetric under the reflection $\mathcal{R}$. The antisymmetric modes are assumed to arise from von Karman vortex shedding. In addition, as in Ref. [6], we assume that the strength of the von Karman vortices can be quantified by the fractional latency of the antisymmetric coherent structures. The bifurcation diagram, Fig. 8, shows that antisymmetric modes appear as ϕ is reduced below 1.0 and that the latencies contained in the antisymmetric modes increase as ϕ is reduced further. The smooth bifurcation diagram, as compared to the results in Ref. [6], may be attributed to the filtering scheme used in this study.

B. Phase portraits

The onset of von Karman shedding is accompanied by a reorganization in the configuration space defined by $a_n(t)$, $n = 0,1,\ldots,14$. The periodicity, quasiperiodicity, or aperiodicity of an orbit is reflected in the configuration space [4]. In Fig. 9 we use the projection $(a_0(t),a_2(t))$ for visualization. Orbits prior to the onset ($\phi = 1.1,\ 1.04,\ 1.0$) appear to be noisy recurrent orbits, while those following the onset ($\phi = 0.9,\ 0.8,\ 0.7$) are more irregular (perhaps noisy quasiperiodic orbits). The width of the configuration-space orbits is a measure of the strength of irregular motions. The relatively narrow widths of the orbits at high equivalence ratios are attributed to the flame becoming more uniform across the cross-sectional plane of the rig as a result of acoustic coupling with the oscillating pressure field within the rig.

C. Lyapunov exponents

One of the defining characteristics of chaotic or irregular flows is the divergence of nearby points in configuration space of the flow [4]. Typically, the largest deviations are along the direction of the flow. Lyapunov exponents [4,13], which quantify the mean expansion of the dynamics along and across the flow, can be used as a measure of the "irregularity" of the flow. Lyapunov exponents and their dependence on the equivalence ratio are computed using techniques introduced in Ref. [37]. We limit consideration to projections to the

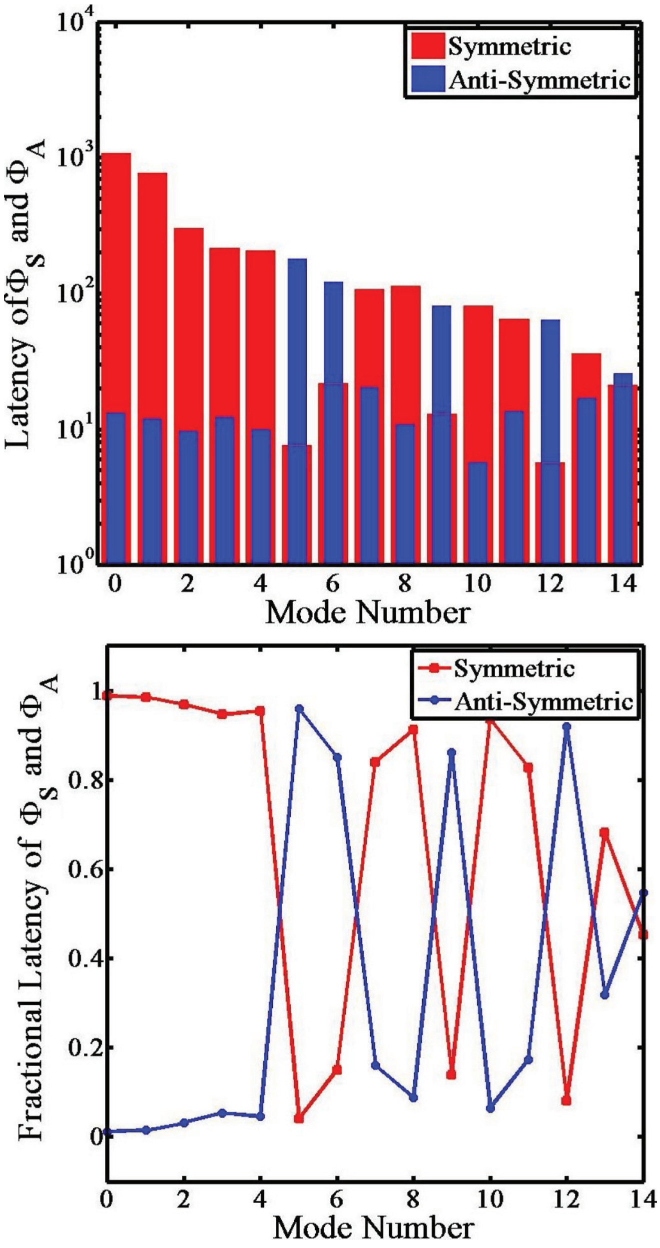

FIG. 7. (Color online) (a) Latency and (b) fractional latency of symmetric and antisymmetric components of coherent structures 0–14 for the flow at $\phi = 0.8$. Note that the dominant components of modes 5, 6, 9, and 12 are antisymmetric, suggesting the presence of von Karman vortex shedding.

$(a_0(t),a_2(t))$ plane. (Variations of the exponent with the equivalence ratio do not depend on this choice.) We choose a small patch of the plane and identify points $\mathbf{x}_i$ of the orbit within it. The point $\mathbf{x}_i$ evolves to a point $\mathbf{y}_i$ (in a different patch) during the next time step (0.0001 s). We assume that the evolution of $\mathbf{x}_i \rightarrow \mathbf{y}_i$ can be approximated by a (locally) linear transformation $\mathcal{L}$, which is estimated by minimizing the least-squares difference of $(\mathbf{y}_i - \mathbf{y}_j)$ and $\mathcal{L}(\mathbf{x}_i - \mathbf{x}_j)$, for all pairs of points $\mathbf{x}_i$ and $\mathbf{x}_j$ in the original patch. Now we follow an orbit, constructing patches at each time step and computing the associated linearizations. The Lyapunov exponent is the logarithm of the largest eigenvalue of the product (per step) as the orbit length increases.

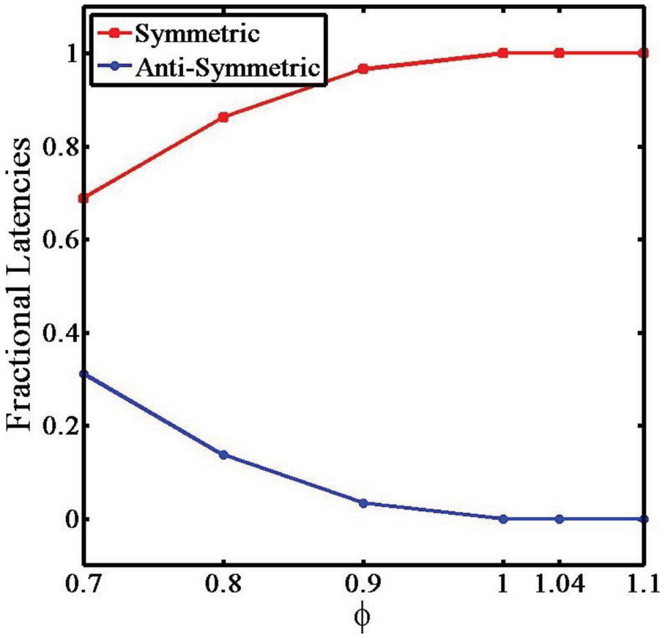

FIG. 8. (Color online) Bifurcation diagram for onset of von Karman vortex shedding.

Figure 10 shows the variation in the Lyapunov exponent for the flow as the equivalence ratio is changed. The onset of von Karman vortex shedding is accompanied by an increase in the Lyapunov exponent, i.e., neighboring points on the phase diagram diverge faster following the transition.

Fractal properties [38] of an attractor can be used to characterize chaotic motions. However, the correlation dimension [39,40] of all attractors shown in Fig. 9 are found to be close to 2. Thus, due to experimental noise and irregular small-scale facets, it is not possible to derive fractal characterizations of our flow.

VI. PERIODIC ORBITS IN THE FLOW

The computation of (unstable) periodic orbits will be illustrated in the context of bluff-body stabilized flames. As shown below, we find only one periodic orbit prior to the onset of von Karman vortex shedding and two following the transition. Interestingly, the period of the cycle prior to the transition is ~8 ms, which is representative of the 125-Hz acoustically coupled flame frequency. The presence of such rapid flow components highlights the critical need for high-frequency imaging.

A. Preliminaries

Periodic orbits within the flow are most easily identified using a *Poincaré section*. Qualitative analysis of a dynamical system can be simplified by limiting consideration to intersections of the state-space orbit with a lower dimensional subspace (Poincaré section) that intersects it transversly; i.e., the section is not tangent to the orbit. The map from one such intersection (passing from a given side of the Poincaré section to the other) to the next is referred to as a *Poincaré map* [4,41] (see Fig. 11).

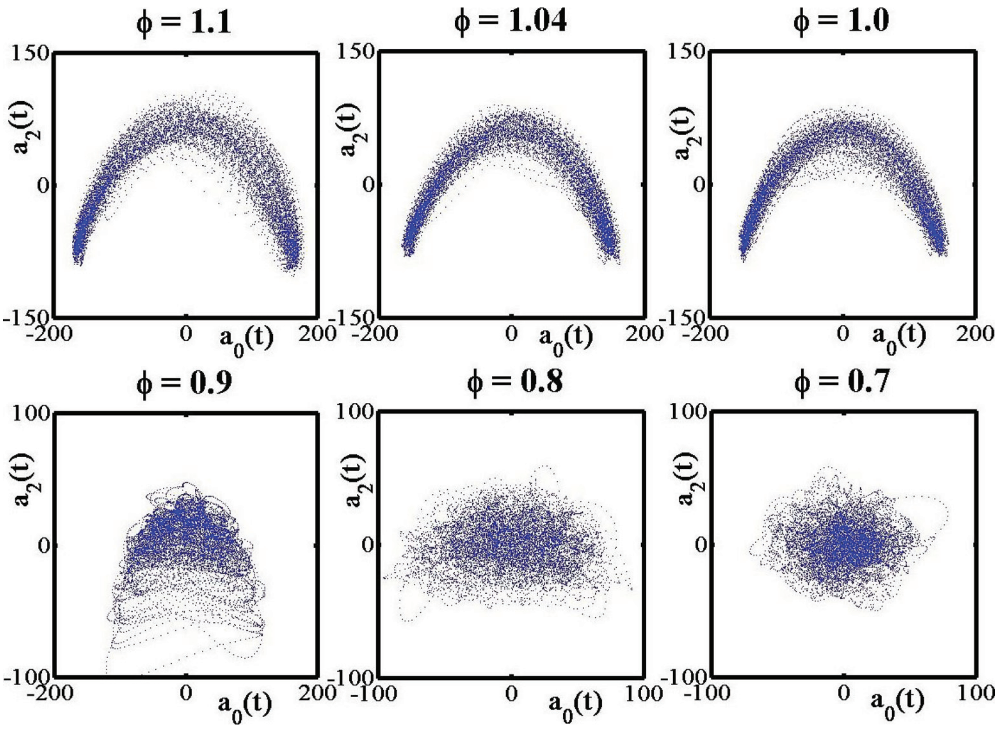

FIG. 9. (Color online) Changes in phase portrait [here the projection to $(a_0(t),a_2(t))$] as ϕ changes from 1.1 to 0.7. Transition to the onset of von Karman vortices is accompanied by the change of the phase portrait from an inverted-U structure to a filled-loop structure. Similar changes are observed in other projections as well.

The Poincaré map is discrete and has one less dimension than the flow.

In Fig. 11 we provide two schematic examples. Figure 11(a) presents a two-dimensional periodic flow and a Poincaré section $y = 0$. The flow intersects the section at the same point $\mathcal{P}_0$ repeatedly; $\mathcal{P}_0$ is a fixed point of the Poincaré map. The one-dimensional flow has been reduced to a zero-dimensional map. The second example, illustrated in Fig. 11(b), is a quasiperiodic flow on a torus. Its intersections with the Poincaré section lie on a circle, and the Poincaré map is quasiperiodic on the circle (i.e., similar to an irrational rotation). Here, the two-dimensional, quasiperiodic flow has been reduced to a one-dimensional, quasiperiodic Poincaré map. Similarly, a chaotic flow will be reduced to a chaotic map of one less dimension on the Poincaré section, and the (closure of the) intersection will be a strange attractor [4].

Being unstable, periodic orbits are not directly observable; their presence and location must be inferred from the flow. To perform this task, we first note that nearby points in chaotic or irregular flows will diverge (the “butterfly effect”). The divergence is large along one direction, the mean growth rate being the (first) Lyapunov exponent [13]; typically, the divergence of the flow normal to the chaotic attractor (or the second Lyapunov exponent) is smaller. Consequently, an orbit that approaches close to a fixed point on the Poincaré section will maintain proximity to the corresponding periodic orbit of the flow for a finite time interval. Hence, a point sufficiently close to a fixed point of a Poincaré map is likely to make a close return [14,23]. We search for all such close returns on the Poincaré section. Typically, such points cluster into a few groups, each of which is assumed to be associated with a fixed point of the Poincaré map; the fixed point is estimated to be the centroid of the cluster [23].

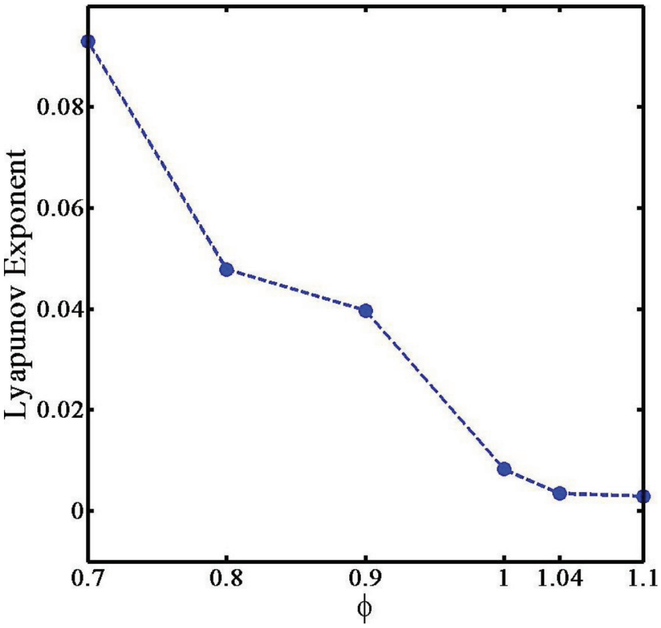

FIG. 10. (Color online) Lyapunov exponent of the flow in the range of equivalence ratios studied. Note that the exponent increases with the onset of von Karman vortex shedding.

B. Periodic orbits for $\phi = 1.1$

We select the Poincaré section $a_1(t) = 0$ for our analysis and search for crossings from $a_1 < 0$ to $a_1 > 0$. The data

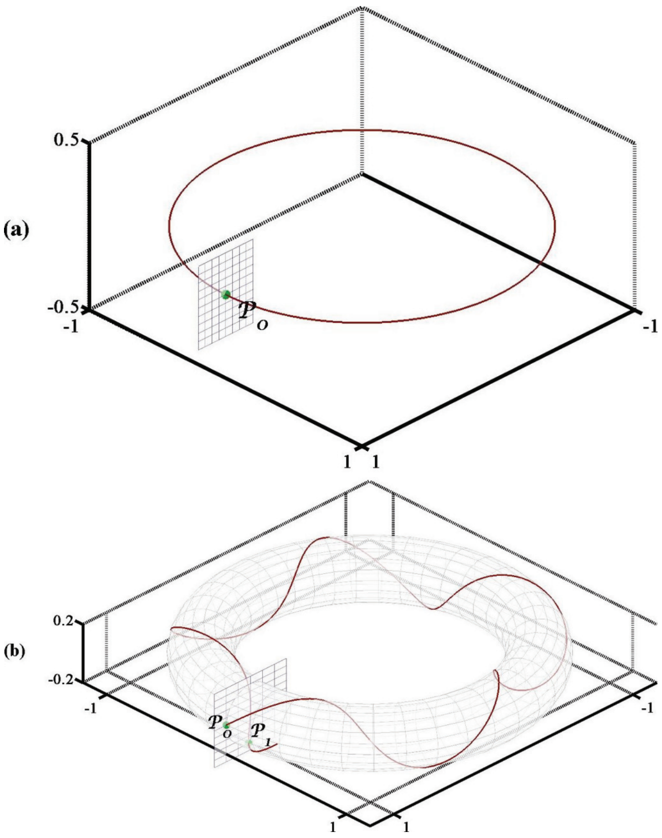

FIG. 11. (Color online) Schematic examples of Poincaré maps for flows. (a) Periodic orbit of the flow intersects a single point $\mathcal{P}_0$ on the Poincaré section repeatedly; $\mathcal{P}_0$ is a fixed point of the Poincaré map. (b) Quasiperiodic orbits of the flow intersects the Poincaré section on a curve. Two successive crossings $\mathcal{P}_0$ and $\mathcal{P}_1$ are shown. The Poincaré map $\mathcal{P}_0 \to \mathcal{P}_1$ is quasiperiodic.

(which are available only on a discrete set of time points, i.e., the frames) are interpolated using a third-order spline to estimate the crossing time t_c. The value of each remaining coefficient $a_n(t_c)$ $(n = 0,2,\ldots,14)$ at the crossing is also computed using a spline fit.

Our analysis was conducted on the reduced-order flow defined by using the first 15 coherent structures. Close returns on the Poincaré section are defined as orbits that return to within a prespecified distance $\varepsilon = 0.01$ from the first crossing. (Identical periodic orbits are found for a range of ε values.) Figure 12(a) shows the intersections of the periodic (or quasiperiodic) orbit of the flow (at $\phi = 1.1$) with the Poincaré section. When there is a close return, we mark the first crossing with a red circle and its iterate with a green triangle. Each such pair is connected by a dashed line. The blue open circles denote crossings whose iterates (i.e., next crossings) do not fall within ε. We find seven close returns of the Poincaré map. Notice that all seven first crossings (red circles) are clustered in one neighborhood; we assume that the proximity of their returns is due to the presence of a fixed point on the Poincaré section, and its location is estimated by the mean of the seven first crossings.

Next, we discuss an inference that can be made on the basis of the presence of only one periodic orbit in the flow. If the flow were chaotic, one would expect multiple periodic orbits to be embedded in the attractor and the orbit to follow distinct cycles in the course of the flow [14,15,18]. In this scenario, several periodic orbits would have been extracted by our algorithm.

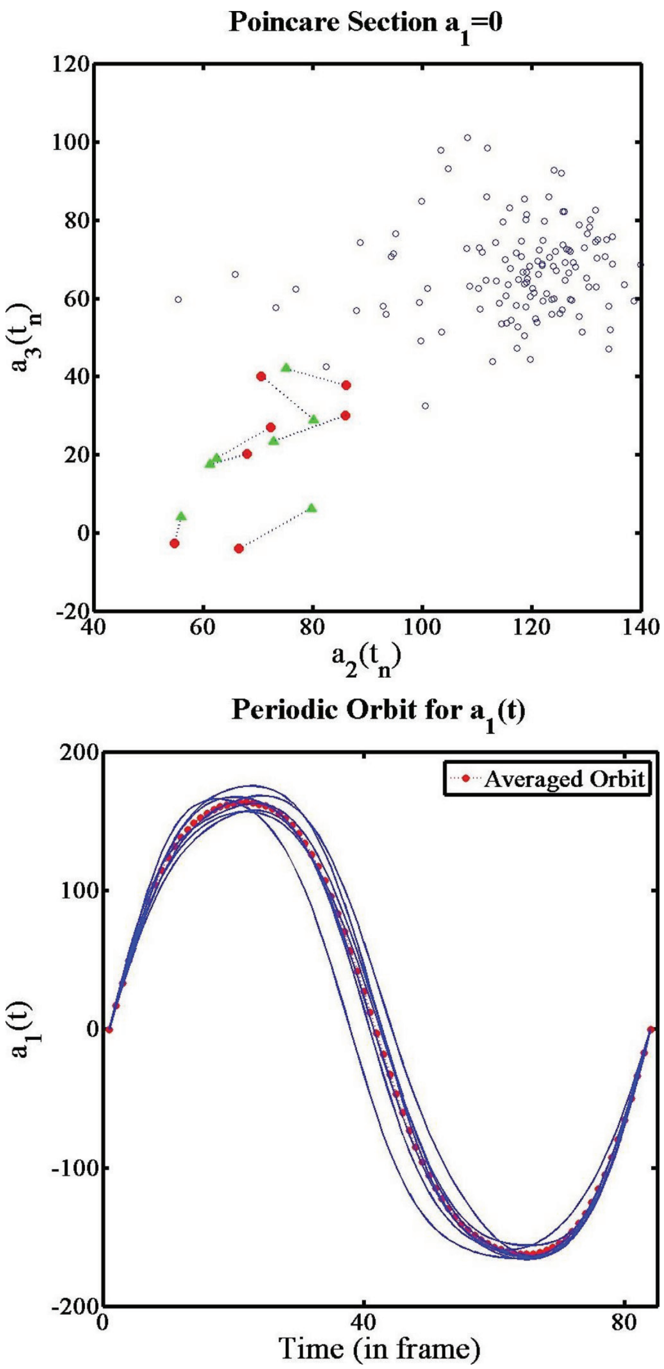

FIG. 12. (Color online) (a) Intersections of the flow at $\phi = 1.1$ with the Poincaré section $a_1 = 0$. First crossings for close returns, defined by $\varepsilon = 0.01$, are shown by red closed circles, while returns to the section are shown by green closed triangles. Dashed lines join pairs of first crossings and returns; i.e., represent the Poincaré map. Open circles are the remaining crossings of the orbit with the Poincaré section, whose returns are farther than ε from the first crossing. (b) Dynamics of $a_1(t)$ between the first crossing and return for the seven close returns identified in (a). All seven appear to be organized around a single periodic orbit. The cycle, marked by red circles, is estimated to be the mean of the seven close returns.

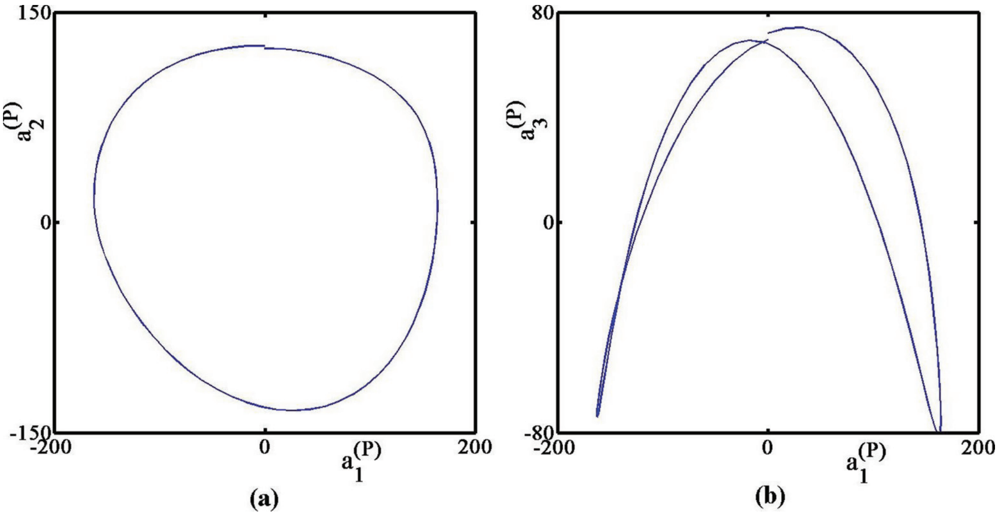

FIG. 13. (Color online) Projections of the periodic orbit of the flow at $\phi = 1.1$ to the (a_1,a_2) and (a_1,a_3) planes.

Our inability to find more than one orbit is the first indication that the large-scale flow, in the absence of noise and other irregular facets, is periodic and not chaotic; it also confirms that our flame oscillations are indeed acoustically coupled to the experimental rig.

Next, we consider the flows emanating from each of the seven first crossings [red circles in Fig. 12(a)] and compute their dynamics at regular time intervals (using spline-fits as necessary). The dynamics of $a_1(t)$ for the seven orbits are shown in Fig. 12(b). The proximity of the seven orbits justifies our assumption that the close returns are caused by a single neighboring periodic orbit. The location of the periodic orbit $a_1^{(P)}(t)$ at time t is assigned as the centroid of the seven orbits at t. (Note that the periods of the seven close returns, although similar, are not identical. To compute the cycle, we linearly scale the period of each orbit so all orbits have a common period.) The estimated periodic orbit is shown by red circles in Fig. 12(b). Figure 13 displays two projections of the recurrent orbit.

Analysis of the remaining flows prior to the onset of von Karman vortices (i.e., at $\phi = 1.04$ and $\phi = 1.0$) yields qualitatively similar results. Specifically, we find only one cycle in each case, and as can be seen from Fig. 14 for $\phi = 1.04$, the periodic orbits for the three cases are qualitatively similar.

C. Periodic orbits for $\phi = 0.8$

Poincaré sections for each flow beyond the onset of von Karman vortices (i.e., $\phi < 1.0$) show two clusters of close returns. A periodic orbit is associated with each cluster. Furthermore, the pairs of orbits for all equivalance ratios beyond the onset are qualitatively similar. Figure 15 shows the same pair of projections for each cycle for the flow at $\phi = 0.8$.

Beyond the onset of von Karman vortices, the flow is organized around two periodic orbits. Figures 15(a) and 15(b) show two projections of the first cycle and Figs. 15(c) and 15(d) those of the other. Notice that the orbits do not close precisely because the centroid of the locations of the first crossings of

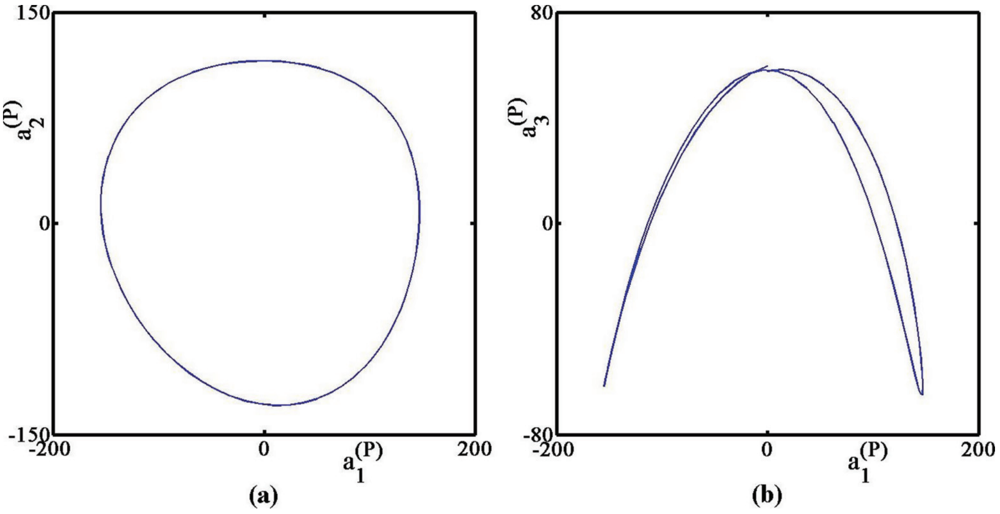

FIG. 14. (Color online) Projections of the periodic orbit of the flow at $\phi = 1.04$ to the (a_1,a_2) and (a_1,a_3) planes. Note that the projections are qualitatively similar to those for the flow at $\phi = 1.1$ (see Fig. 13).

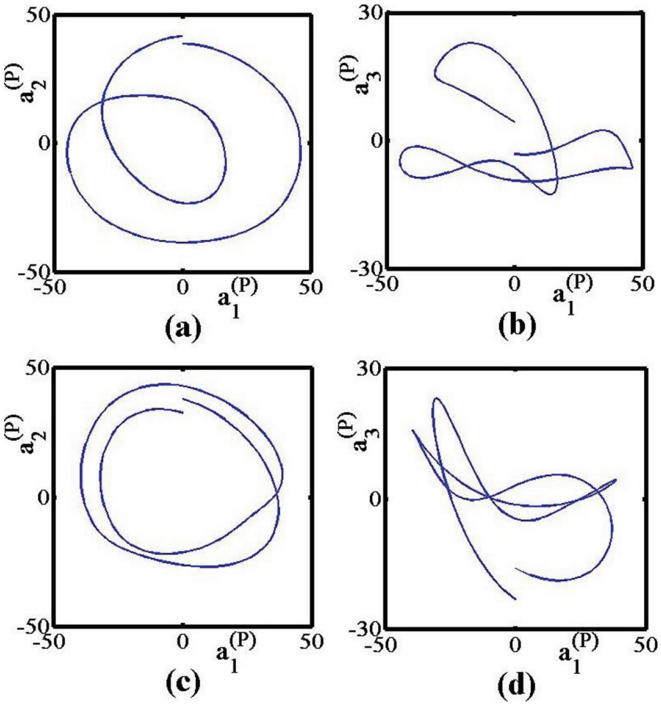

FIG. 15. (Color online) Projections of two periodic orbits of the flow at $\phi = 0.8$ to the (a_1,a_2) and (a_1,a_3) planes. (a) and (b) show projections of one cycle and (c) and (d) those of the other.

the close returns are, although nearby, not identical to those of the images.

D. Unstable periodic orbits for the flow

Thus far, we have the computed periodic orbits of the reduced model defined from the dynamics of the coefficients $a_n^{(P)}(t)$ of the first 15 coherent structures. An approximation to the corresponding flow itself can be derived using Eq. (2), i.e.,

$$U_P(\mathbf{x},t) \approx \sum_{n=0}^{15} a_n^{(P)}(t)\Phi(\mathbf{x}). \qquad (7)$$

Figure 16 provides snapshots (at the same time) to compare the original flow and the periodic (or recurrent) flow (i.e., the flow computed from the recurrent orbit). Note that the original flow contains small-scale structures and other irregular features, while the recurrent flow exhibits neither. In fact, a video of the same recurrent flow, provided in the Supplemental Materials, shows an extremely clean flow that returns to its initial state following the shedding of a symmetric pair of vortices.

The flame flow following the onset of von Karman vortices (i.e., for $\phi < 1$) can be de-convoluted in the same manner. Figures 17(a) and 17(b) show a snapshot of the flow at $\phi = 0.8$ and the corresponding snapshot of the recurrent flow. Observe that the periodic flow does not have up-down symmetry. Figures 17(c) and 17(d) show the symmetric and antisymmetric components of the latter.

The reconstruction of the periodic flow allows us to characterize the noise and some other irregular features of the flow (an alternative to looking at PCA reconstruction in Ref. [6]). Specifically, the irregular facets can be defined as the difference between the original flow and the recurrent flow within the duration of the cycle. Figure 18 contains snapshots of the difference for four close returns used in computing the periodic flow at $\phi = 1.1$. Specifically, we consider four close returns and select a prespecified point

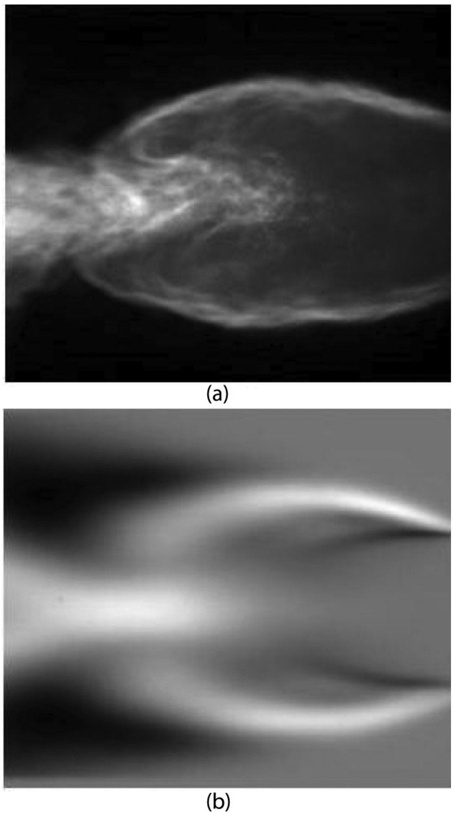

FIG. 16. Simultaneous snapshots of (a) the original flow at equivalence ratio $\phi = 1.1$ and (b) recurrent flow. Note that the former contains noise and other irregular small-scale structures. The size of the images is approximately 100 × 66 mm.

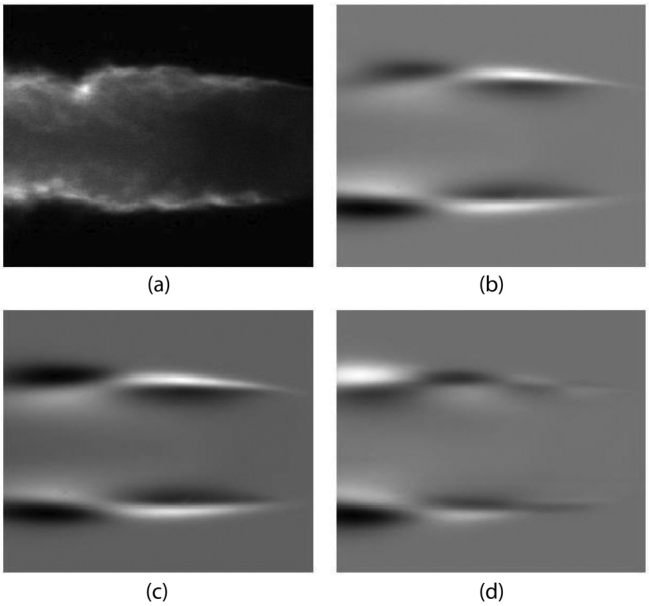

FIG. 17. Simultaneous snapshots of (a) the flow at equivalence ration $\phi = 0.8$ and (b) recurrent flow. Symmetric and antisymmetric components of the latter are given in (c) and (d), respectively.

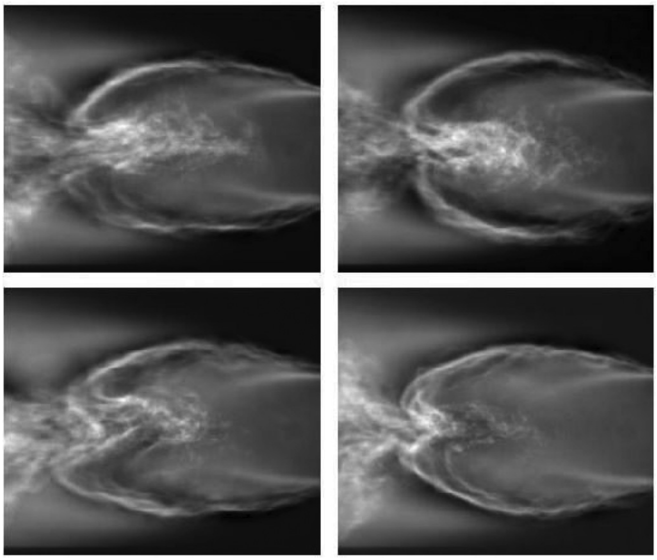

FIG. 18. Differences in images from equivalent time points of four close returns and corresponding snapshots of periodic flow at $\phi = 1.1$. Images represent noise and other irregular facets of the flow. Note that the images have "similar" statistical features, but the precise structures depend on the close return.

in state space (see Fig. 13). We identify the corresponding snapshot of the flow and subtract the image of the recurrent flow from it. Two observations are in order: (1) The irregular motion is concentrated near the flow locations of large velocity gradients. This is to be expected since small-scale structures are generated by energy cascading, which is concentrated at locations with high velocity gradients, and (2) the precise deviations from the periodic flow depend on the specific close return analyzed. This justifies our nomenclature—irregular motion—for these small-scale facets of the flow. However, all four images appear to have similar qualitative features.

One of the remaining tasks is to provide a comprehensive (and quantitative) statistical characterization of these irregular structures and their dynamics. We have conducted a pair of standard tests. First, the spectrum for the noise decays as a power law in frequency, suggesting that the small-scale structures are not governed by low-dimensional chaos [42]. Second, PCA of the corresponding spatiotemporal dynamics shows a slow decay of the latencies. Thus, a large number of coherent structures is needed to provide a good approximation to the noise. This pair of results indicates that the small-scale irregular flows are either stochastic or governed by high-dimensional dynamics.

VII. FLOW BEHIND OTHER SYMMETRIC BLUFF BODIES

We highlight a collection of results derived from the analysis of reacting flows behind bluff bodies of other (symmetric) shapes. The analyses are identical to that described in Secs. III–VI. Flow characteristics remain unchanged, but the strength of the irregularities differs, being smallest for the v-gutter bluff body.

Figure 19 displays the bifurcation diagrams for the flow behind (a) cylindrical, (b) flat, (c) square, and (d) v-gutter bluff bodies. In each case, the estimated onset of von Karman vortices occurs at an equivalence ratio between $\phi = 1.0$ and $\phi = 0.9$. However, the growth of the antisymmetric component following the onset (i.e., smaller ϕ) is smallest for the v-gutter and largest for the square flame holder. This may suggest that the bluff body in the shape of the v-gutter perturbs the flame flow minimally as the equivalence ratio is reduced below the onset of von Karman vortex shedding. Another factor that may be contributing to the shapes of the curves in Fig. 19 is the acoustic coupling. It appears that, for square and cylindrical flame holders, the transition to acoustically coupled flames does not begin for $\phi < 0.7$ and $\phi < 0.8$, respectively. Differences in the downstream pressure field may prevent the coupling of the flames at these low equivalence ratios. However, once the equivalence ratio is increased, the transition to acoustically coupled conditions appears to be more abrupt. This sensitivity to equivalence ratio may prove to be problematic for active control systems that may not have sufficient time to alter upstream conditions to reduce or prevent the coupling. The frequency bandwidth of the pressure and heat-release fluctuations may be used in the future to understand how the differences in coupling could be caused by the overlap.

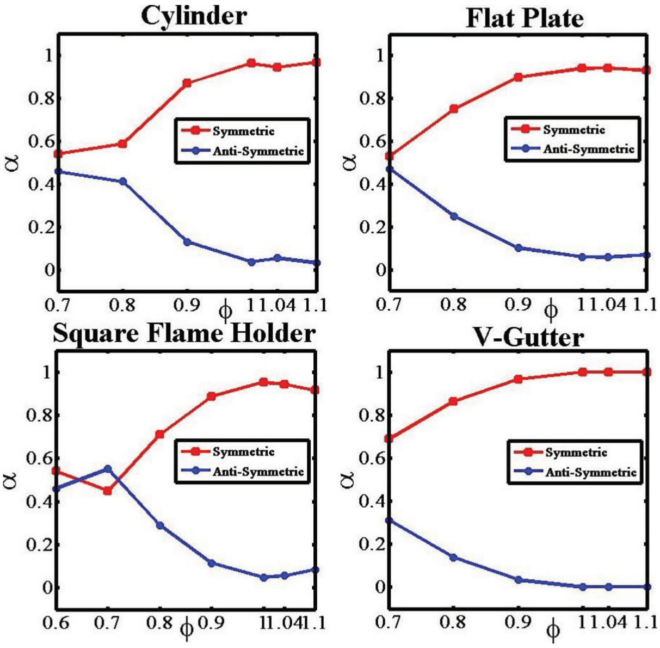

FIG. 19. (Color online) Bifurcation diagrams for onset and growth of von Karman vortex shedding with decreasing ϕ for bluff bodies of several shapes. In each case the bifurcation appears between equivalence ratios $\phi = 0.9$ and $\phi = 1.0$.

Figure 20 shows projection to the (a_0,a_2) and (a_0,a_3) planes of the phase portrait prior to (i.e., larger ϕ) and following (i.e., smaller ϕ) the onset of von Karman vortex shedding for the four bluff bodies. Once again, it appears that the symmetric flow behind the v-gutter contains the lowest level of noise. The low noise in the v-gutter is in agreement with the fact that the symmetric energy for the v-gutter is highest in Fig. 21 (see below). This suggests that heat-release fluctuations and shedding behind the v-gutter couple best with the pressure fluctuations in the rig. The remaining bluff-body shapes with more irregular shedding (symbolized by phase

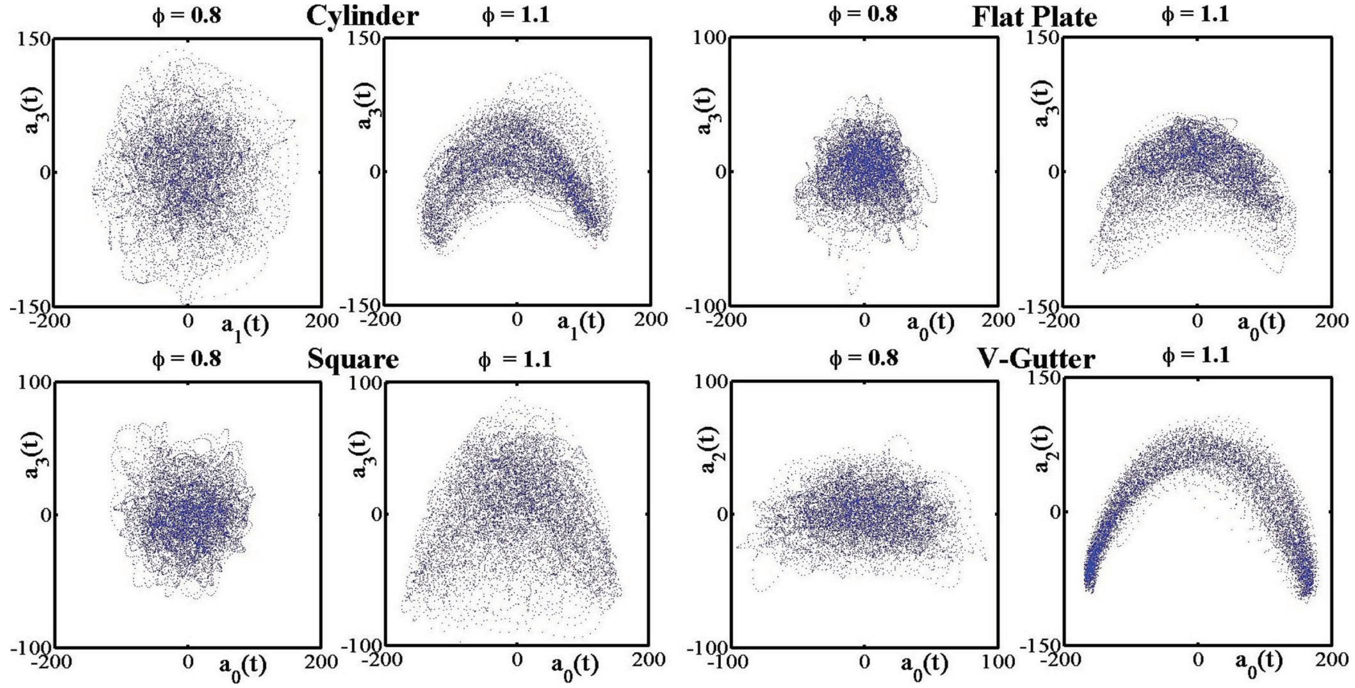

FIG. 20. (Color online) Projections to a subspace defined by two eigenvectors illustrate changes of the phase portrait prior to and following the onset of von Karman vortex shedding for four bluff bodies. Images suggest that the flow behind the v-gutter contains the least noise or irregularities.

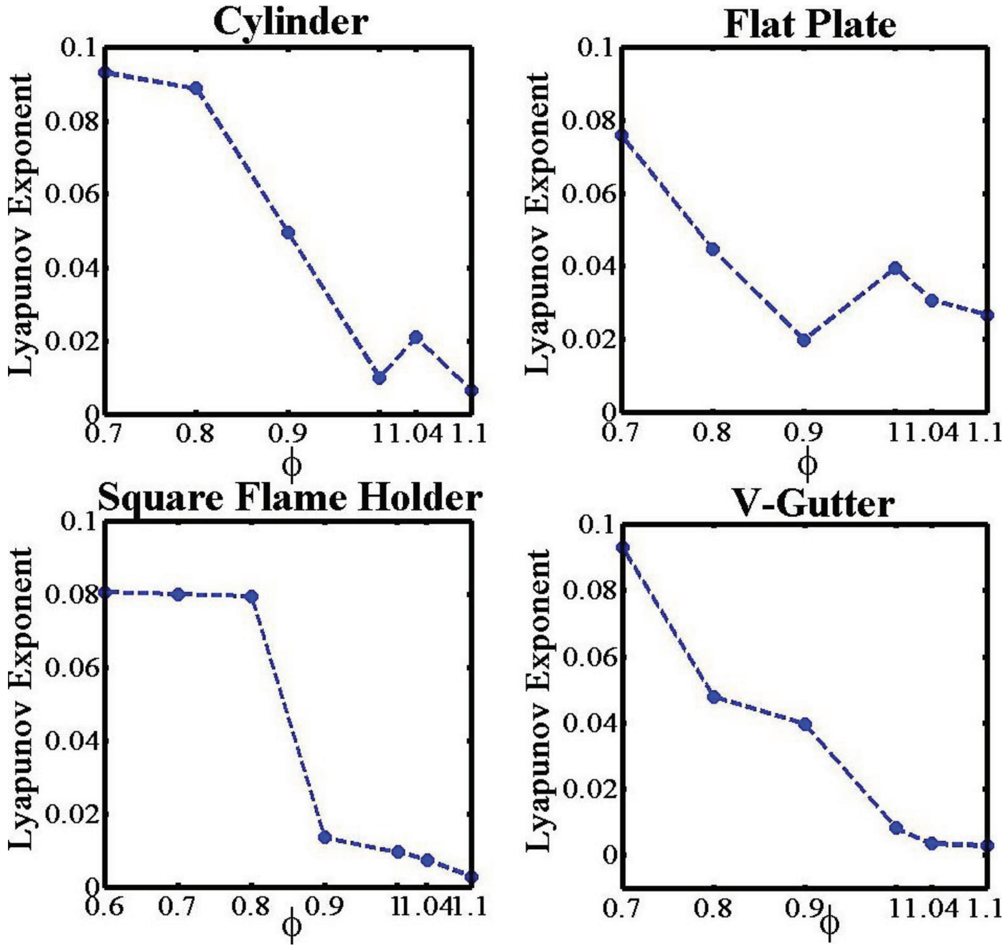

FIG. 21. (Color online) Growth of Lyapunov exponents for flow behind four bluff bodies as the equivalence ratio is reduced. Expansion rates for flow behind cylindrical, square, and v-gutter bluff bodies are similar. Flow behind the flat plate shows different behavior.

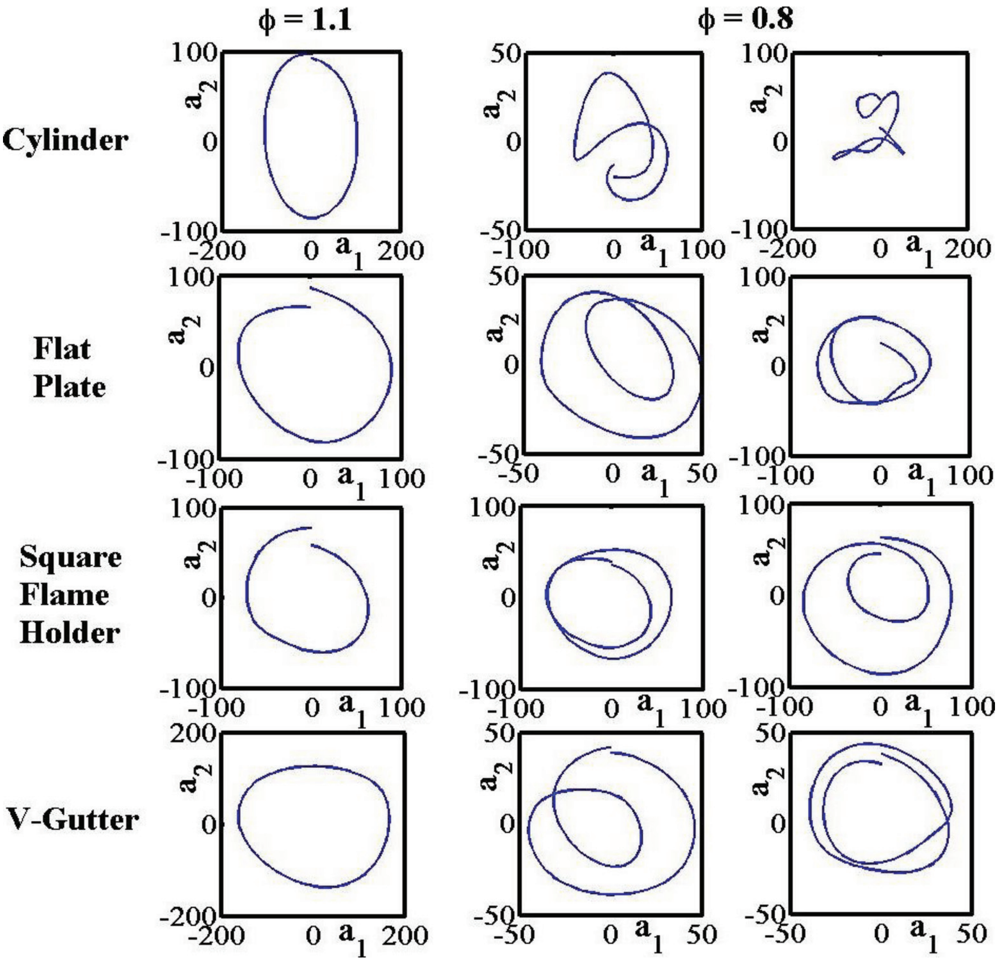

FIG. 22. (Color online) Periodic orbits prior to and subsequent to the onset of von Karman vortex shedding for the flow behind the four bluff bodies.

portraits with more irregularity) probably inherently provide additional damping of the acoustics [43].

The flows behind all symmetric bluff bodies exhibit similar qualitative behavior both prior to and subsequent to the onset of von Karman vortex shedding, as can be observed from the phase portraits (Fig. 20), Lyapunov exponents (Fig. 21), and periodic orbits (Fig. 22), although the second set of cycles for the flow behind the cylinder appear different. However, the flow behind the v-gutter exhibits the least irregularity, confirming a more efficient coupling of the flame heat release with the acoustic field in the rig.

We find a larger number of close returns for the flow behind the v-gutter, which once again suggests that this flow is the most regular. In addition, periodic orbits for the flow behind other bluff bodies fail to make (sufficiently) close returns. For example, for $\phi = 1.1$, we find five, four, and four close returns for the flow behind the cylindrical, flat, and square bluff bodies, respectively. We find only two periodic orbits for each flow following the onset, and they are similar for the flat plate, the square flame holder, and the v-gutter. The orbits for the lower equivalence ratio in Fig. 22 also suggest that the cylindrical flame holder provides the least amount of acoustic coupling since the returns are farthest away there. However, we find the same number of periodic orbits [one prior to the onset (i.e., large φ) and two following the onset (i.e., small φ)] for the flow behind each bluff body.

VIII. DISCUSSION AND CONCLUSIONS

Enhancing the performance of combustion systems such as engines requires designs to minimize or delay flow instabilities. Unfortunately, higher efficiencies occur in leaner fuel-air mixtures—the very regime where flow instabilities are initiated. Theoretical approaches to addressing these issues encounter serious obstacles. Fundamental equations of fluid dynamics and chemical kinetics are nonlinear, and flow characteristics depend sensitively on their precise form and the values of control parameters and boundary conditions. Perturbation approaches also fail to yield reliable results in intensely driven nonlinear systems. In contrast, experimental techniques, particularly methods for extracting ultra-high-frequency, high-resolution flow patterns, have undergone rapid advances in recent years. Thus, the need is critical for data-based reduced-order models to analyze and control flow instabilities.

In this study, we introduced a modal decomposition of bluff-body-stabilized combustion flows. The energy in these flows is introduced through large-scale external actions, acoustic instabilities, or vortex shedding. In addition, the flow contains irregular, small-scale motions created through viscous-mediated energy cascading. These small-scale motions feed back and impose irregularities on the large-scale flows as well. Some of the questions that motivated our study were as follows: (1) Are large-scale flows regular in the absence of feedback from the small scales? (2) If so, can transitions in these flows be identified and characterized? (3) What are the statistical descriptions appropriate to the small-scale flows?

We focused on high-momentum combustion behind bluff bodies under conditions that include symmetric vortex shedding. As the equivalence ratio of the mixture is reduced, the flow undergoes a transition beyond which the flow sheds von Karman vortices as well [6]. Since von Karman modes are observed at small equivalence ratios and will only increase with the upstream temperatures [44], their onset may signal the limits in optimizing the efficiency of engines, and designs that delay their onset may prove useful in enhancing engine efficiency.

The methods outlined in this paper are extensions of the proper orthogonal decomposition introduced in Ref. [6]. All experimental systems we analyzed had a reflection symmetry about an axis along the flow direction. Symmetric vortex shedding retains this symmetry, while von Karman shedding breaks it. Our deconvolution of the flow relied on this observation: First, when the vortex shedding is symmetric, all coherent structures in the expansion are necessarily symmetric under reflection; hence, any asymmetry in the computed coherent structures is due to noise and irregular feedback from the small-scale motions. This observation provides a measure of the irregular motions and an algorithm for filtering them. Second, when the flow contains von Karman shedding as well, the strength of these vortices can be quantified by the antisymmetric components of the coherent structures.

These assertions were used to identify the onset and growth of von Karman vortex shedding. The onset is illustrated with bifurcation diagrams and qualitative changes in the phase-space orbits. The growth of von Karman modes is characterized using bifurcation diagrams and Lyapunov exponents. We further characterized the transition by computing the (unstable) periodic orbits embedded in the flow. We found only one such orbit prior to the onset of von Karman vortices and a pair of orbits following the transition.

The presence of only one or two periodic orbits in the flow has an important consequence. If the flows were chaotic, one would expect multiple periodic orbits to be embedded in the attractor [14,15,18], and our algorithm would have yielded several periodic orbits. Our inability to find more than one orbit prior to the transition suggests that the large-scale flow is periodic (not chaotic) and that the irregular facets of the flow probably result from feedback from the small scales. The vanishing of the Lyapunov exponent for $\phi \geqslant 1$ provides additional evidence for the periodicity of the large-scale flow. These results are consistent with estimates made from flow characteristics. The cross-sectional area (approximately 150×125 mm) and the velocity (approximately 14 m/s) provide an estimate of the Reynolds number of 3×10^5, which is below the transition to turbulent flow for a cylindrical barrier [45], once again suggesting that the primary flame flow is not irregular.

We conducted the analysis for bluff-body-stabilized flow behind flame holders of four (symmetric) shapes. The qualitative features for the flows are similar in each case, although the level of irregularity depends on the specific shape of the flame holder. We found that the onset of von Karman shedding occurs at (nearly) the same equivalence ratio. However, the flow behind a v-gutter is least irregular and that behind the cylindrical bluff body is most irregular. This observation may assist in optimizing engine design.

Knowledge of the relevant coherent structures and their symmetries can be used to infer the normal-form equations for the underlying spatiotemporal dynamics [4,12,46]. These normal forms can be used to predict secondary bifurcations in the system [46,47]. Such analyses have been conducted for many fluid systems, including cellular flame patterns [48,49].

Periodic orbits within an irregular flow are especially useful in controlling a chaotic flow [50,51]. The crucial observation is that since the cycle is embedded in the irregular orbit, it requires only a small perturbation to guide a chaotic system toward the periodic orbit [52,53]. Furthermore, since the requisite perturbations are small, one may assume that superposition applies; once responses of the system to a collection of perturbations are established, they can be superposed in an appropriate way to obtain a prespecified response of the system. The method has been successfully applied to control systems as diverse as reaction–diffusion systems [54], flame fronts [54], lasers [55], magnetoelastic ribbons [56], cardiac rhythms [57–60], and brain signals [61]. One of our future goals is to validate that periodic orbits within the flow can be used to reduce or eliminate irregular facets of bluff-body-stabilized flames.

The motivation for our work was to deconvolute the complex flame flow into its constituents. In our studies we explicitly used differences in the symmetries between symmetric and von Karman vortex shedding to identify flow patterns associated with each mode. Such partitioning is required because individual structures consists of a combination of coherent structures rather than a single structure. Unfortunately, this approach cannot differentiate two or more modes with the same symmetry and cannot be used to analyze physical systems (e.g., jet engines) with no symmetry. One option is to use the frequency content of the dynamics to identify coherent structures to be combined into each flow component. Another possibility is to use dynamical mode decomposition [34,35].

ACKNOWLEDGMENTS

G.H.G. thanks Predrag Cvitanović for discussions on periodic orbits. Funding for this research was provided by the Air Force Office of Scientific Research (Dr. Chiping Li, Program Manager) and by the Air Force Research Laboratory under Contracts No. FA8650-12-C-2200 and No. FA8650-12-M-2283. This manuscript has been cleared for public release by the Air Force Research Laboratory (No. 88ABW-2013-1163).

[1] S. Chandrasekhar, *Hydrodynamic and Hydromagnetic Stability* (Dover, New York, 1961).
[2] P. G. Drazin and W. H. Reid, *Hydrodynamic Stability* (Cambridge University Press, Cambridge, 1981).
[3] T. Lieuwen, J. Propul. Power **19**, 765 (2003).
[4] M. Cross and P. Hohenberg, Rev. Mod. Phys. **65**, 851 (1993).
[5] A. C. Noble, G. B. King, N. M. Laurendeau, J. R. Gord, and S. Roy, Combust. Sci. Technol. **184**, 293 (2012).
[6] S. Kostka, A. C. Lynch, B. C. Huelskamp, B. V. Kiel, J. R. Gord, and S. Roy, Combust. Flame **159**, 2872 (2012).
[7] T. Maxworthy, Combust. Flame **6**, 233 (1962).
[8] S. Chaudhuri, S. Kostka, M. W. Renfro, and B. M. Cetegen, Combust. Flame **157**, 790 (2010).
[9] J. Hertzberg, I. Shepherd, and L. Talbot, Combust. Flame **86**, 1 (1991).
[10] L.-Z. Huang and D.-M. Nie, Thermal Science **16**, 1395 (2012).
[11] E. Konstantinidis and S. Balabani, J. Fluids Struct. **23**, 1047 (2007).
[12] M. Golubitsky, D. G. Schaffer, and I. Stewart, *Singularities and Groups in Bifurcation Theory* (Springer-Verlag, Berlin, 1988), Vol. 2.
[13] J. Froyland, Phys. Lett. A **97**, 8 (1983).
[14] P. Cvitanović, Phys. Rev. Lett. **61**, 2729 (1988).
[15] D. Auerbach, P. Cvitanović, J.-P. Eckmann, G. Gunaratne, and I. Procaccia, Phys. Rev. Lett. **58**, 2387 (1987).
[16] P. Cvitanovic and Y. H. Lan, *Correlations and Fluctuations in QCD*, edited by N. G. Antoniou, F. K. Diakonos, and C. N. Ktorides, 10th International Workshop on Multiparticle Production, Iraklion, Greece (World Scientific, Singapore, 2002).
[17] Y. Lan and P. Cvitanović, Phys. Rev. E **69**, 016217 (2004).
[18] P. Cvitanović, G. H. Gunaratne, and I. Procaccia, Phys. Rev. A **38**, 1503 (1988).
[19] G. H. Gunaratne and I. Procaccia, Phys. Rev. Lett. **59**, 1377 (1987).
[20] G. H. Gunaratne, M. H. Jensen, and I. Procaccia, Nonlinearity **1**, 157 (1988).
[21] P. Cvitanovic, *Nonlinear Physical Phenomena*, edited by A. Ferraz, F. Oliveira, and R. Osorio, School on Nonlinear Physical Phenomena, Brasilia, Brazil (World Scientific, Singapore, 1989).
[22] G. H. Gunaratne, P. S. Linsay, and M. J. Vinson, Phys. Rev. Lett. **63**, 1 (1989).
[23] A. L. Belmonte, M. J. Vinson, J. A. Glazier, G. H. Gunaratne, and B. G. Kenny, Phys. Rev. Lett. **61**, 539 (1988).
[24] M. Slutzky, P. Cvitanovic, and D. Mogul, Ann. Biomed. Eng. **29**, 607 (2001).
[25] M. Slutzky, P. Cvitanovic, and D. Mogul, J. Neurosci. Methods **118**, 153 (2002).
[26] J. L. Lumley, *The Structure of Inhomogeneous Flow*, Atmospheric Turbulence and Radio Wave Propagation (Nauka, Moscow, 1967), pp. 166–176.
[27] G. Berkooz, P. Holmes, and J. Lumley, Annu. Rev. Fluid Mech. **25**, 539 (1993).
[28] G. Berkooz, P. Holmes, and J. L. Lumley, *Turbulence, Coherent Structures, Dynamical Systems, and Symmetry*, Cambridge Monographs on Mechanics (Cambridge University Press, Cambridge, UK, 1996).
[29] M. N. Glauser, S. J. Leib, and W. K. George, Turbulent Shear Flows **5**, 134 (1987).
[30] L. Sirovich, Q. Appl. Math. **45**, 561 (1987).
[31] L. Sirovich, Q. Appl. Math. **45**, 573 (1987).
[32] L. Sirovich, Q. Appl. Math. **45**, 583 (1987).
[33] P. Petersson, R. Wellander, J. Olofsson, H. Carlsson, C. Carlsson, B. B. Watz, N. Boestkjaer, M. Richter, M. Alden, L. Fuchs, and X.-S. Bai, *Simultaneous High-Speed PIV and OH PLIF Measurements and Modal Analysis for Investigating Flame-Flow Interactions in Low Swirl Flames*, in 16th International Symposium on Applications of Laser Techniques to Fluid Mechanics, Lisbon, Portugal (http://ltces.dem.ist.utl.pt/lxlaser/lxlaser2012/, 2012).
[34] P. J. Schmid, J. Fluid Mech. **656**, 5 (2010).
[35] P. J. Schmid, *Dynamic Mode Decomposition of Experimental Data*, in 8th International Symposium on Particle Image Velocimetry-PIV09, Melbourne, Victoria (Springer-Verlag, Berlin, 2009).
[36] M. Bergmann, C. H. Bruneau, and A. Lollo, J. Comput. Phys. **228**, 516 (2009).
[37] A. Wolf, J. Swift, H. Swinney, and J. Vastano, Physica D **16**, 285 (1985).
[38] B. Mandelbrot, Science **156**, 636 (1967).
[39] P. Grassberger and I. Procaccia, Physica D **9**, 189 (1983).
[40] P. Grassberger and I. Procaccia, Phys. Rev. Lett. **50**, 346 (1983).
[41] G. Teschl, *Ordinary Differential Equations and Dynamical Systems*, Graduate Studies in Mathematics (American Mathematical Society, Providence, RI, 2012), Vol. 140.
[42] M. Gorman, M. el Hamdi, and K. Robbins, Combust. Sci. Technol. **98**, 47 (1994).
[43] T. Lieuwen and J. Cho, J. Sound Vib. **279**, 669 (2005).
[44] P. Mehta, M. Soteriou, and A. Banaszuk, Combust. Flame **141**, 392 (2005).
[45] F. P. Incropera, D. P. deWitt, T. L. Bergman, and A. S. Lavine, *Fundamentals of Heat and Mass Transfer* (John Wiley & Sons, Hoboken, NJ, 1990).
[46] P. Coullet and G. Iooss, Phys. Rev. Lett. **64**, 866 (1990).
[47] G. Dangelmayr and D. Armbruster, Proc. Lond. Math. Soc. **46**, 517 (1983).
[48] A. Palacios, G. Gunaratne, M. Gorman, and K. Robbins, Chaos **7**, 463 (1997).
[49] A. Palacios, M. Gorman, and G. Gunaratne, Chaos **9**, 755 (1999).
[50] A. L. Fradkov and R. J. Evans, Ann. Rev. Cont. **29**, 33 (2005).
[51] S. Narayanan and F. Hussain, *Chaos Control in Open Flows: Experiments in a Circular Jet*, Proceedings of the Fourth AIAA Shear Flow Control Conference, Snowmass, CO (American Institute of Aeronautics and Astronautics, Reston, VA, 1997).
[52] E. Ott, C. Grebogi, and J. A. Yorke, Phys. Rev. Lett. **64**, 1196 (1990).
[53] T. Shinbrot, C. Grebogi, E. Ott, and J. Yorke, Nature **363**, 411 (1993).
[54] V. Petrov, M. Crowley, and K. Showalter, J. Chem. Phys. **101**, 6606 (1994).
[55] R. Roy, T. Murphy, T. Maier, Z. Gills, and E. Hunt, Phys. Rev. Lett. **68**, 1259 (1992).
[56] V. In, W. Ditto, and M. Spano, Phys. Rev. E **51**, R2689 (1995).
[57] A. Garfinkel, W. Ditto, M. Spano, and J. Weiss, Circulation **86**, 217 (1992).

[58] A. Garfinkel, M. Spano, W. Ditto, and J. Weiss, Science **257**, 1230 (1992).

[59] A. Garfinkel, J. Weiss, W. Ditto, and M. Spano, Trends Cardiovasc. Med. **5**, 76 (1995).

[60] K. Hall, D. Christini, M. Tremblay, J. Collins, L. Glass, and J. Billette, Phys. Rev. Lett. **78**, 4518 (1997).

[61] S. Schiff, K. Jerger, D. Duong, T. Chang, M. Spano, and W. Ditto, Nature **370**, 615 (1994).